IJMMM International Journal of Minerals, Metallurgy and Materials 矿物冶金与材料学报（英文版）

Effect of ball milling time on the microstructure and compressive properties of the Fe–Mn–Al porous steel

Lingzhi Xie, Zhigang Xu, Yunzhe Qi, Jinrong Liang, Peng He, Qiang Shen, and Chuanbin Wang

Cite this article as:
Lingzhi Xie, Zhigang Xu, Yunzhe Qi, Jinrong Liang, Peng He, Qiang Shen, and Chuanbin Wang, Effect of ball milling time on the microstructure and compressive properties of the Fe–Mn–Al porous steel, *Int. J. Miner. Metall. Mater.*, 30(2023), No. 5, pp. 917-929. https://doi.org/10.1007/s12613-022-2568-3

International Journal of Minerals, Metallurgy and Materials
Volume 30, Number 5, May 2023, Page 917
https://doi.org/10.1007/s12613-022-2568-3

Effect of ball milling time on the microstructure and compressive properties of the Fe–Mn–Al porous steel

Lingzhi Xie[1,3], *Zhigang Xu*[1,2)✉], *Yunzhe Qi*[1)], *Jinrong Liang*[1)], *Peng He*[4)], *Qiang Shen*[2)], *and Chuanbin Wang*[2)]

1) Hubei Key Laboratory of Advanced Technology for Automotive Components, Wuhan University of Technology, Wuhan 430070, China
2) State Key Lab of Advanced Technology for Materials Synthesis and Processing, Wuhan University of Technology, Wuhan 430070, China
3) School of Materials Science and Engineering, Wuhan University of Technology, Wuhan 430070, China
4) Wuhan Second Ship Design and Research Institute, Wuhan 430205, China
(Received: 29 July 2022; revised: 30 October 2022; accepted: 31 October 2022)

Abstract: In the present work, Fe–Mn–Al–C powder mixtures were manufactured by elemental powders with different ball milling time, and the porous high-Mn and high-Al steel was fabricated by powder sintering. The results indicated that the powder size significantly decreased, and the morphology of the Fe powder tended to be increasingly flat as the milling time increased. However, the prolonged milling duration had limited impact on the phase transition of the powder mixture. The main phases of all the samples sintered at 640°C were α-Fe, α-Mn and Al, and a small amount of Fe_2Al_5 and Al_8Mn_5. When the sintering temperature increased to 1200°C, the phase composition was mainly comprised of γ-Fe and α-Fe. The weight loss fraction of the sintered sample decreased with milling time, i.e., 8.3wt% after 20 h milling compared to 15.3wt% for 10 h. The Mn depletion region (MDR) for the 10, 15, and 20 h milled samples was about 780, 600, and 370 μm, respectively. The total porosity of samples sintered at 640°C decreased from ~46.6vol% for the 10 h milled powder to ~44.2vol% for 20 h milled powder. After sintering at 1200°C, the total porosity of sintered samples prepared by 10 and 20 h milled powder was ~58.3vol% and ~51.3vol%, respectively. The compressive strength and ductility of the 1200°C sintered porous steel increased as the milling time increased.

Keywords: powder metallurgy; porous steel; ball milling time; microstructure evolution; compressive properties

1. Introduction

Porous steels, as a good candidate for structural and functional performance, offer a variety of outstanding advantages such as high mechanical [1–4], corrosion [5–7], thermal [8], acoustic [9–10], electromagnetic shielding/absorbing properties [11–12], and excellent economical availability [13]. Currently, many solid-state and liquid-state routes including powder metallurgy [14–15], casting [16], directional solidification of metal/gas eutectics (GASAR) [17], electrodeposition [18], dealloying [19–20], and additive manufacturing [21–24], have been widely used to produce porous steels. Among them, powder metallurgy is a well-received technique to prepare porous steels due to the unique merits of the short processing cycle, tailorable composition, low preparation temperature, uniform composition, and controllable pore features.

Ball milling is an important way to achieve powder refinement. In the process of ball milling, powders are collided and squeezed by the pellets, causing severe plastic deformation, cold welding, and fracture [25–26]. Many researches reveal that the milling time has a great influence on the particle size and morphology of the powder [25,27–29]. Generally, the powder size decreases with the extension of milling time before reaching a limit value. The particle size and morphology of the powder are key factors affecting the pore structure and mechanical properties of porous steels [24,30–31]. Due to the difference of the surface energy, lattice distortion, and atomic diffusion distance, powders with different particle size have different densification after sintering, which could affect the mechanical properties of the porous steels.

At present, the base materials for fabricating steel foams are mainly stainless steels and carbon steels [9,10,12,32–33]. Compared with the frequently employed steel matrix, steels with high-Mn (20wt%–40wt%) and high-Al content (5wt%–20wt%) have lower density and better mechanical properties [20]. That is to say, the high-Mn and high-Al steels as the parent steel can further reduce weight and improve the mechanical properties of the porous steels [34–35]. However, the previous reported synthesizing porous steels are mostly prealloyed steel powder [3,30–31]. Prealloyed powder presents a fix chemical composition, which goes against to tuning the chemical composition in real time in the alloy design. In addition, the manufacturing cost of the prealloyed steel powder is much higher than that of the elemental

✉ Corresponding author: Zhigang Xu E-mail: zhigangxu@whut.edu.cn

powder. Thus, it is worthwhile to synthesize porous steels using elemental powder as raw materials. Previously, we employed elemental powders of Fe, Mn, Al, and C as raw materials to produce a high-Mn and high-Al porous steel with large porosity through a novel two-step vacuum sintering strategy comprised of the diffusion/reactions between different elements and the sublimation of Mn. Then, the influence of the sintering temperature on the microstructure evolution and pore formation mechanism are concerned [2,4,36–37]. However, there are few works to demonstrate the effect of the milling time on the microstructure and mechanical properties of porous high-Mn and high-Al steel using elemental powders as raw materials. This work, for the first time, used elemental powders of Fe, Mn, Al, and C to produce powder mixture with different features by different ball milling durations, and discussed the influence of the milling time on the microstructure and compressive properties of the porous high-Mn and high-Al steel, which provides a theoretical basis for the performance optimization and the application of the high-Mn and high-Al porous steel.

2. Experimental

2.1. Raw materials and sample preparation

Elemental pure Fe powder (43 μm in median size), pure Mn powder (40 μm in median size), pure Al powder (38 μm in median size), and C powder (5 μm in median size) were used as raw materials. The morphology of the original powder was shown in Fig. 1, where the Fe, Mn, Al, and C particles were rounded, angular, spherical, and flake in shape, respectively. The nominal composition of the powder mixture was Fe–35wt% Mn–10wt% Al–1wt% C. The mixed powder was ball milled in a stainless steel (SS) vial with SS balls as milling medium for 10, 15, and 20 h, respectively. More details on the preparation of the ball milled powder are available in published work [2,37]. The milled powder was cold compacted under a uniaxial pressure of 200 MPa. Subsequently, the green samples were sintered in a furnace with a vacuum degree of ≤5.0×10^{-3} Pa. Two batches of samples were sintered at 640 and 1200°C for 60 min with a heating rate of 5°C·min^{-1}, respectively, followed by furnace cooling.

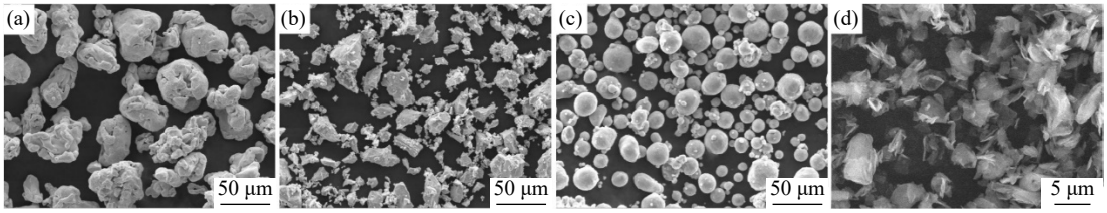

Fig. 1. SEM images of the original powders: (a) Fe; (b) Mn; (c) Al; (d) C.

2.2. Testing and characterization

The phase compositions were identified by X-ray diffraction analysis (Empyrean, PANalytical B.V., Netherlands) with Cu K_α radiation at a scanning speed of 2°·min^{-1} at room temperature. Scanning electron microscopy (SEM, FEI Quanta FEG 450, U.S.) combined with energy-dispersive spectrometry (EDS) was employed to characterize the microstructure and composition of the sintered compacts. The microanalysis of the elemental distribution of the sintered samples was performed by Electron Probe Micro-Analyzer (EPMA, JXA8530F, Japan). GASA software was used to fit the crystal structure of the full XRD spectrum, and the mean size of the ball milled powder was estimated according to the Scherrer formula. The porosity of the sintered compacts was determined according to ASTM B962–17. The weight loss fraction was defined as $(w_0 - w_1) / w_0 \times 100\%$, where w_0 was the mass of the green samples, while w_1 was the mass of the sintered samples [37]. The compression test was performed on a universal materials-testing machine with a compression speed of 0.5 mm·min^{-1}. Cylindrical samples with the diameter of ~13 mm and height of ~17 mm were used for the compression test.

3. Results and discussion

3.1. Microstructure characterizations

Fig. 2 shows the morphology of the 10 h milled powder mixture. It can be seen from Fig. 2(a) and (b) that the size of the Al powder was reduced to 20–30 μm. Meanwhile, a small amount of Al powder was even refined to about 2 μm, as shown in Fig. 2(g) and (h). Compared with the original Fe powder in Fig. 1, Fig. 2(a)–(d) indicated that Fe particles tended to be flake, and the thickness of the flake Fe was about 7 μm. The main reason is that pure Fe powder has a low yield strength and excellent plasticity, which is prone to plastic deformation under the impact of the SS balls. Fig. 2(g) and (h) revealed that Mn particles was significantly refined after milling for 10 h, where many Mn particles were reduced to ~2 μm. Compared with Fe and Al, Mn particles were more brittle and more likely to break up, resulting in the decreasing of Mn particle size. Fig. 2(d)–(f) shows that cold welding occurs between fine particles, where fine Mn particles were embedded on the surface of the flat Fe particles, which are beneficial to shorten the diffusion distance between Fe and Al atoms.

Fig. 3 shows the morphology of the 15 h ball milled powder mixture. The Fe powder became flat with large aspect ratio after continuous cyclic plastic deformation, cold welding, and fracture processes, as shown in Fig. 3(a) and (b). Fig. 3(c)–(e) implied that some Mn particles were further refined to 200–300 nm with elongated morphology. Furthermore, there were many fine Mn and Al particles with a size of about 200 nm embedded on the flat Fe matrix with the thickness of ~6.72 μm (Fig. 3(f)–(h)).

Fig. 4 shows the morphology of the 20 h ball milled

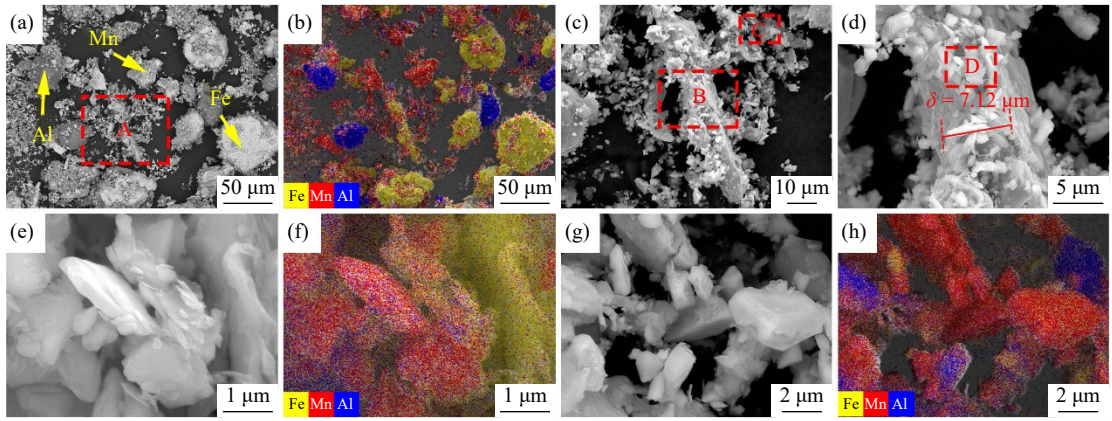

Fig. 2. SEM images and EDS analysis of the powder mixture after 10 h milling: (a, b) morphology and EDS result; (c) enlarged portion in the box A of (a); (d) enlarged portion in the box B of (c); (e, f) enlarged portion in the box D of (d) and EDS result; (g, h) enlarged portion in the box C of (c) and EDS result.

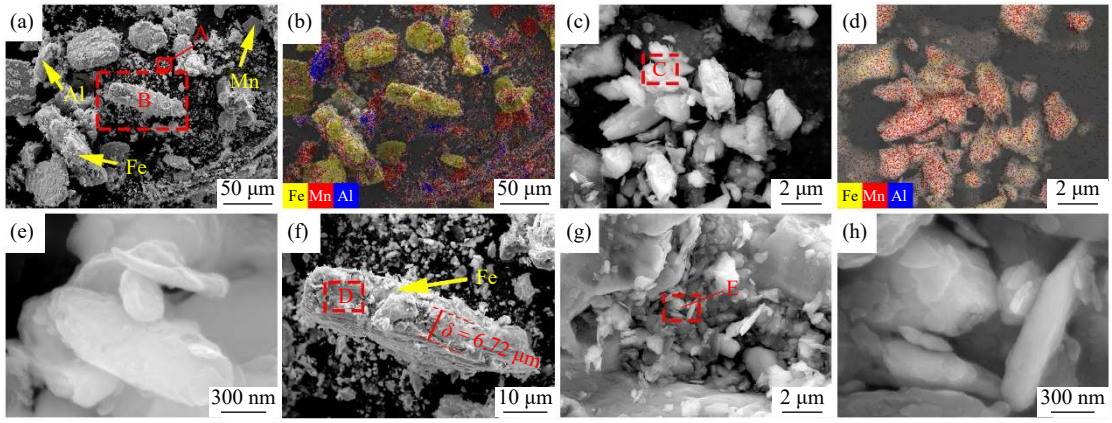

Fig. 3. SEM images and EDS analysis of the powder mixture after 15 h milling: (a, b) morphology and EDS result; (c, d) enlarged portion in the box A of (a) and EDS result; (e) enlarged portion in the box C of (c); (f) enlarged portion in the box B of (a); (g) enlarged portion in the box D of (f); (h) enlarged portion in the box E of (g).

powder mixture. As shown in Fig. 4(a)–(b), a large amount of fine Mn powder was adhered to the flat surface of Fe powder. Fig. 4(c)–(e) presented that there was no much difference in the particle size of the Al and Mn powder between the 20 and 15 h milled powder. This may be because cold welding and agglomeration of particles was intensified the fracture resistance of particles, and increasing the milling time may not provide sufficient energy for further crushing of the particles. In this case, a dynamic balance was established between particle accumulation and fragmentation, resulting in particle size reduction close to the limit. It should be noted that the flattening of Fe particles in the mixed powder was further intensified after 20 h ball milling. The thickness of the Fe flakes was reduced to about 3.62 μm, as shown in Fig. 4(g). Fig. 4(h) and (i) showed that the thickness of some Fe particles was reduced to about 0.73 μm, leading to the specific surface area of Fe particles increased rapidly after 20 h ball milling.

Fig. 5 shows the microstructure of the 10 h milled powder sintered at 640°C. Unreacted Fe, Al, and Mn powder can be observed in Fig. 5(a) and (b). In addition, there were clear boundaries between the most of Fe and Mn particles, and no obvious diffusion was found. This was directly confirmed by EDS line scan result as shown in Fig. 5(g), where the width of the diffusion layer between Fe and Mn particles was only ~0.5 μm, indicating that the diffusion between Fe and Mn particles was limited for the 10 h milled powder sintered at 640°C. The low diffusibility of Fe and Mn particles at this stage may be closely related to the temperature. According to the Fe–Mn binary phase diagram [38], 640°C was not enough to trigger significant diffusion behavior between Fe and Mn particles due to the low solubility (≤ 2wt%) of Mn in α-Fe at 640°C. Fig. 5(c) and (d) implied that many Mn–Al and Fe–Al interdiffusion regions were found in the 10 h milled sample sintered at 640°C, as shown in Fig. 5(e) and (f). It was found that intermetallic compounds Fe_2Al_5 and a small amount of $FeAl_2$ and FeAl existed in the diffusion region of the contacted Fe and Al particles. This was because Al atoms diffused to the Fe matrix and reacted with the supersaturated α-Fe solid solution to form Fe_2Al_5. Subsequently, Fe particles reacted with Fe_2Al_5 to form intermetallic compounds FeAl and $FeAl_2$. Similarly, β-Mn and intermetallic compound Al_8Mn_5 was found in the diffusion region of Mn and Al particles. According to Fe–Al and Mn–Al binary phase diagrams [39–41], Al has high solubility in α-Fe matrix and β-Mn matrix. Therefore, high Al content was detected in α-Fe and β-Mn.

Fig. 6 shows the microstructure of the 15 h milled powder

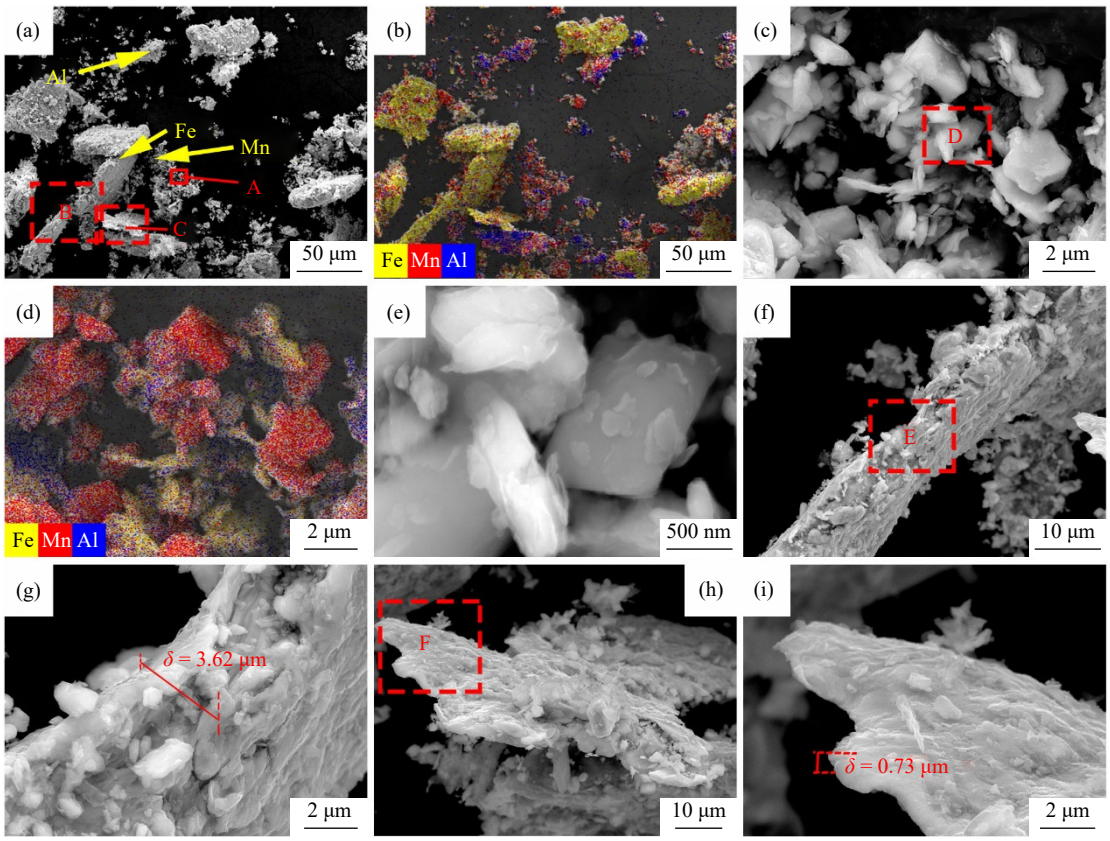

Fig. 4. SEM images and EDS analysis of the powder mixture after 20 milling: (a, b) morphology and EDS result; (c, d) enlarged portion in the box A of (a) and EDS result; (e) enlarged portion in the box D of (c); (f) enlarged portion in the box B of (a); (g) enlarged portion in the box E of (f); (h) enlarged portion in the box C of (a); (i) enlarged portion in the box F of (h).

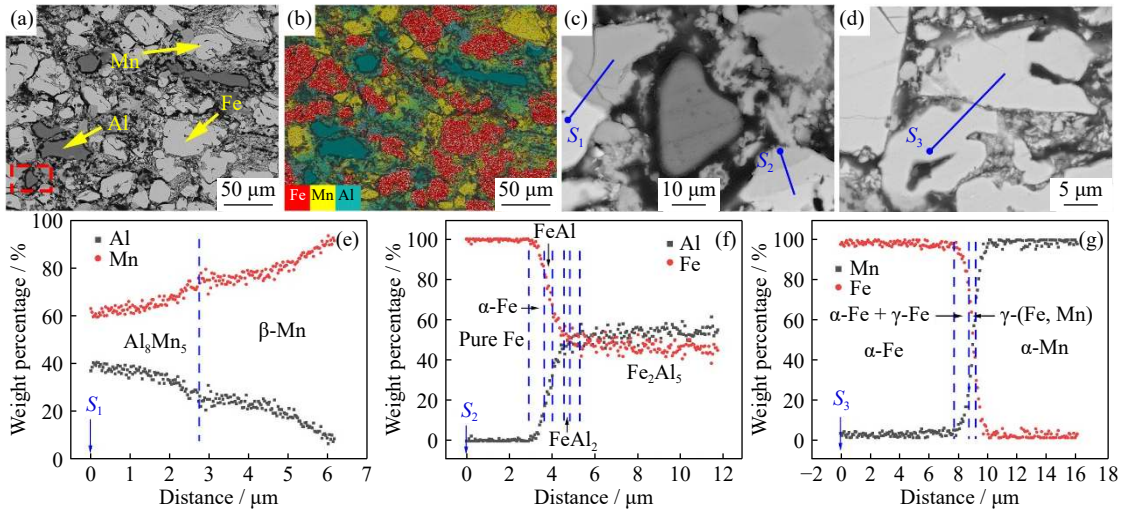

Fig. 5. Microstructure and EDS results of the 10 h milled powder sintered at 640°C: (a, b) SEM image and EDS mapping result; (c, d) partial enlargement of (a); (e–g) EDS line scan results of line S_1, S_2, and S_3, respectively. *S* denotes as the start point of EDS line scan.

sintered at 640°C. It can be clearly seen from Fig. 6(a) and (b) that the residual pure Al particles in the 15 h milled samples were significantly reduced after sintering, revealing that the diffusion of Al was further intensified as more Al particles involved in the diffusion/reaction in the interfacial region of Fe–Al and Mn–Al powder systems, respectively. This can be directly confirmed by the EDS results in Fig. 6(f) and (g), where the diffusion zone between Al–Mn and Al–Fe particles increased to ~11 and ~5 μm, respectively. The wider diffusion zone may be closely related to the smaller size of Al and Mn particles and the thinner Fe particles. This is because the surface energy and defects in the powder increased due to the decrease of the particle size, thereby accelerating elemental diffusion and solid reaction.

As shown in Fig. 7(a) and (b), most of the pure Al particles in the 20 h milled powder were disappeared after sintering, indicating that Al atoms consumed more thoroughly by diffusing and reacting with the surrounding Mn

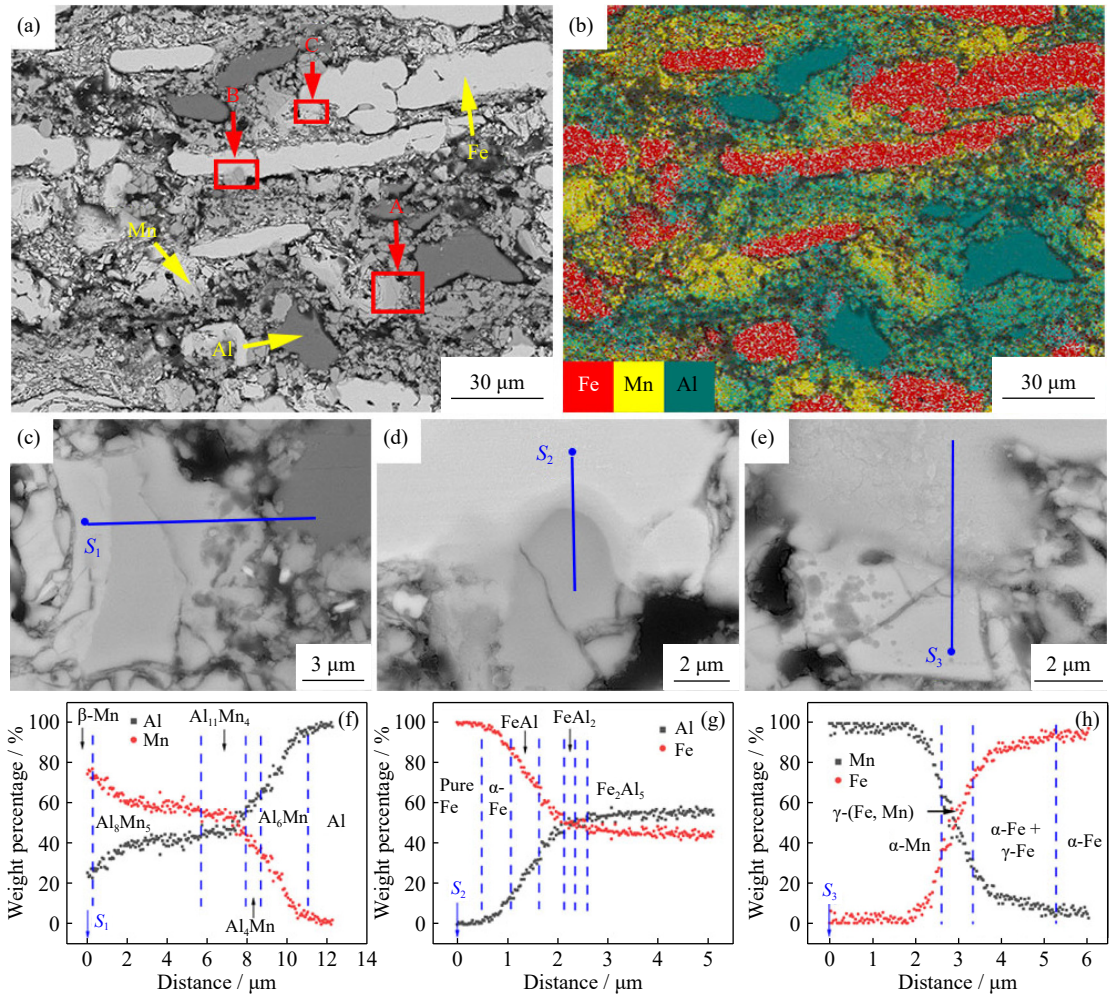

Fig. 6. Microstructure and EDS results of the 15 h milled powder sintered at 640°C: (a, b) SEM image and EDS mapping result; (c–e) the enlargement of boxes A, B, and C in (a), respectively; (f–h) line scan results of lines S_1, S_2, and S_3, respectively. The blue lines in (c–e) are the line scanning area; *S* denotes as the start point of EDS line scan.

particles, and formed Al_8Mn_5 and Al-rich β-Mn phase can be proofed by Fig. 7(f) and (g). Similarly, Al particles reacted with the surrounding Fe particles to form Fe_2Al_5, FeAl, and Al-rich α-Fe phases. The above results implied that the extension of milling time can effectively accelerate the reaction and diffusion.

Fig. 8 shows the microstructure of the milled powder sintered at 1200°C at different mill time. Fig. 8(a) and (b) presented that the overall elemental distribution was uniform, and no pure elements were found. In addition, Fig. 8(a) showed that there were a large number of pores in the sintered body (black area), and most of the pores were interconnected. As shown in Fig. 8(c), component segregation occurred in some particles (small gray regions) with the size of ~2 μm were found in the particles. In addition, there were some small closed pores inside the particles. This may be caused by grain boundary recombination and growth. EPMA results in Fig. 8(h) showed that the grey regions contained high carbon content. A further quantitative analysis identified that the gray regions were κ-carbide, while the white matrix was γ-Fe (see Table 1). According to the Fe–Mn–Al–C phase diagram [42], high Mn content in Fe-based alloys will form γ-Fe phase, which was consistent with the EPMA results.

Fig. 8(i) and (j) showed that there was an obvious particle growth for the sintered 15 h milled powder compared with 10 h milled counterpart, which may be related to the refinement of the powder. In general, the surface energy of the powder gradually increased with the refinement process, leading to the increase of the driving force for particle merging and growth, finally the growth of the sintered particles. The closed pores observed inside the particles were the direct evidence of the particle incorporation. Quantitative EPMA result found that the grey regions in the sintered 15 h milled powder were κ-carbide (see Table 1). Fig. 8(l) and (m) revealed that the morphology of the 20 h milled powder after sintering at 1200°C was more slender, and the slender particles were γ-Fe (see Table 1). It is noted that the morphology of Fe matrix in the powder milled for 20 h was maintained slender throughout all sintering process (i.e., 640 and 1200°C), indicating that the surrounding fine Al and Mn particles preferentially diffused into Fe matrix during sintering process. This is attributed that the fine Al and Mn particles presented larger specific surface than slender iron particles. Thus, Al and Mn particles were incorporated into slender Fe matrix, reducing the surface energy of the system

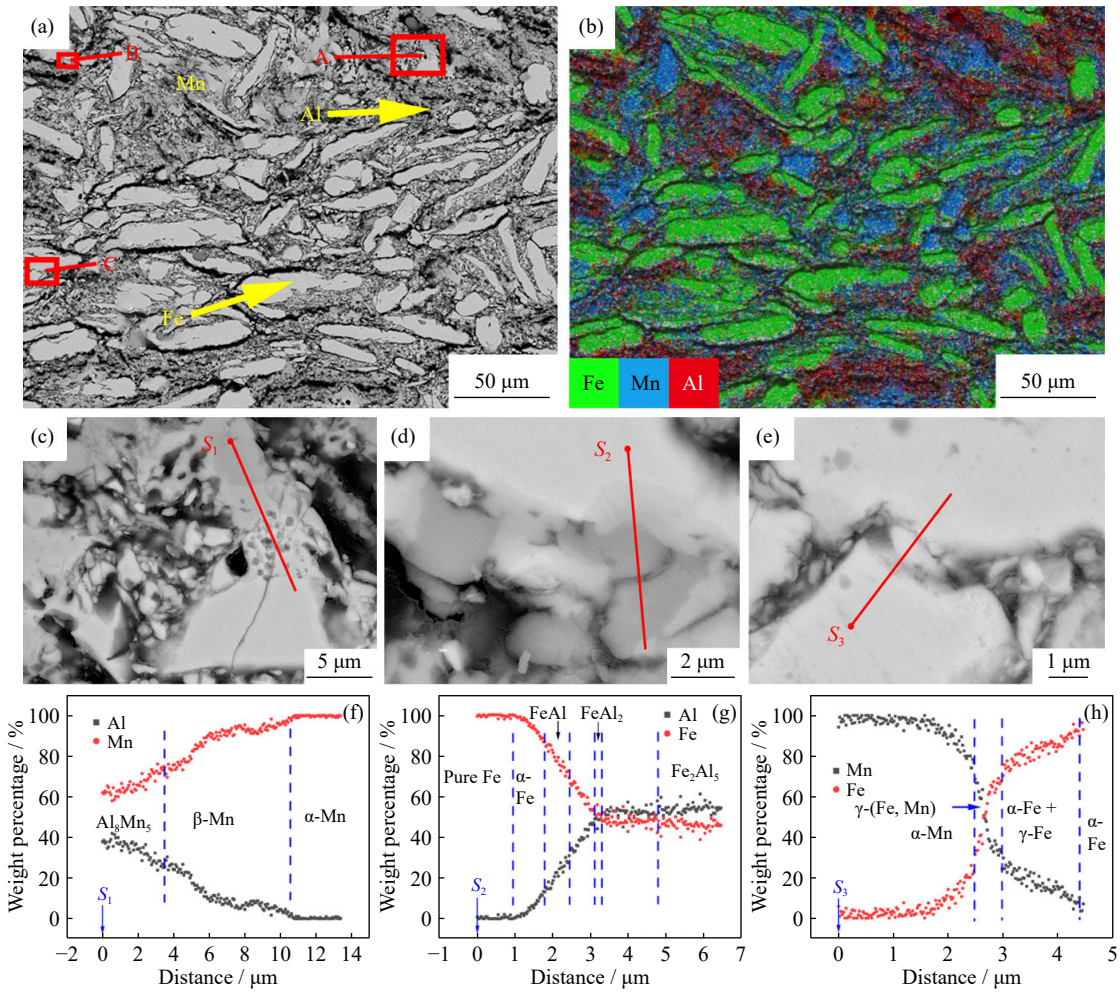

Fig. 7. Microstructure and EDS results of the 20 h milled powder sintered at 640°C: (a, b) SEM image and EDS mapping result; (c–e) the enlargement of boxes A, B, and C in (a), respectively; (f–h) line scan results of S_1, S_2, and S_3, respectively. The red lines in (c–e) are the line scanning area; *S* denotes as the start point of EDS line scan.

and accelerating the process of diffusion and reaction.

3.2. Phase identification

Fig. 9(a) showed that the phase composition of the powder under different milling durations was consistent with the original non-milled powder, indicating that no significant mechanical alloying occurred during milling. Meanwhile, Fig. 9 (b) and (c) revealed that the diffraction peaks of Fe, Mn, and Al broadened with the increase of the balling time, indicating that the grain size decreased as a function of ball milling time. The structural refinement of the diffraction patterns by Rietveld method (Fig. 9(d) and (e)) implied that the average grain size of Fe, Mn, and Al decreased significantly to 55, 25, and 118 nm, respectively, after 20 h milling. This further proved the ball milling process promoted the refinement of the particle size, which agreed to the above-mentioned SEM results.

Fig. 10(a) showed the XRD patterns of the powder with different milling time after sintering at 640°C. There was no obvious change in the phase composition for the samples sintered at 640°C, which mainly consisted of α-Fe, α-Mn, and Al phases. This was consistent with the SEM and EDS results in Figs. 5–7. Futhermore, Fig. 10(b) implied that the diffraction peaks of α-Mn and α-Fe shifted to the low angles, and the deviation of the peaks increased with the increase of milling duration. This demonstrated that the number of the solute atoms in α-Mn and α-Fe boosted with the increase of ball milling durations. According to Fe–Mn and Al–Mn phase diagrams [39–41], the shift of α-Mn peak was mainly caused by the increase of α-Mn lattice constant due to the diffusion of Fe atoms into α-Mn matrix, while the shift of α-Fe peak was mainly caused by the increase of α-Fe lattice constant due to the diffusion of Al atoms into α-Fe. This can be confirmed by the EDS results in Figs. 5–7. The increased diffraction peak offset might be caused by the promoted diffusion of solute atoms in α-Mn and α-Fe due to the continuous refinement of the powder as a function of milling time. When the temperature ramped to 1200°C, α-Mn, β-Mn, and Al phases completely consumed and disappeared as shown in Fig. 10(c). In detail, the 10 h milled powder after sintering at 1200°C was mainly composed of γ-Fe, α-Fe, and a small amount of κ-carbide. For the 15 and 20 h milled powder, only γ-Fe diffraction peak was detected after sintering at 1200°C. This may be attributed that longer milling time was beneficial to the homogenization of the powder system and therefore less composition segregation.

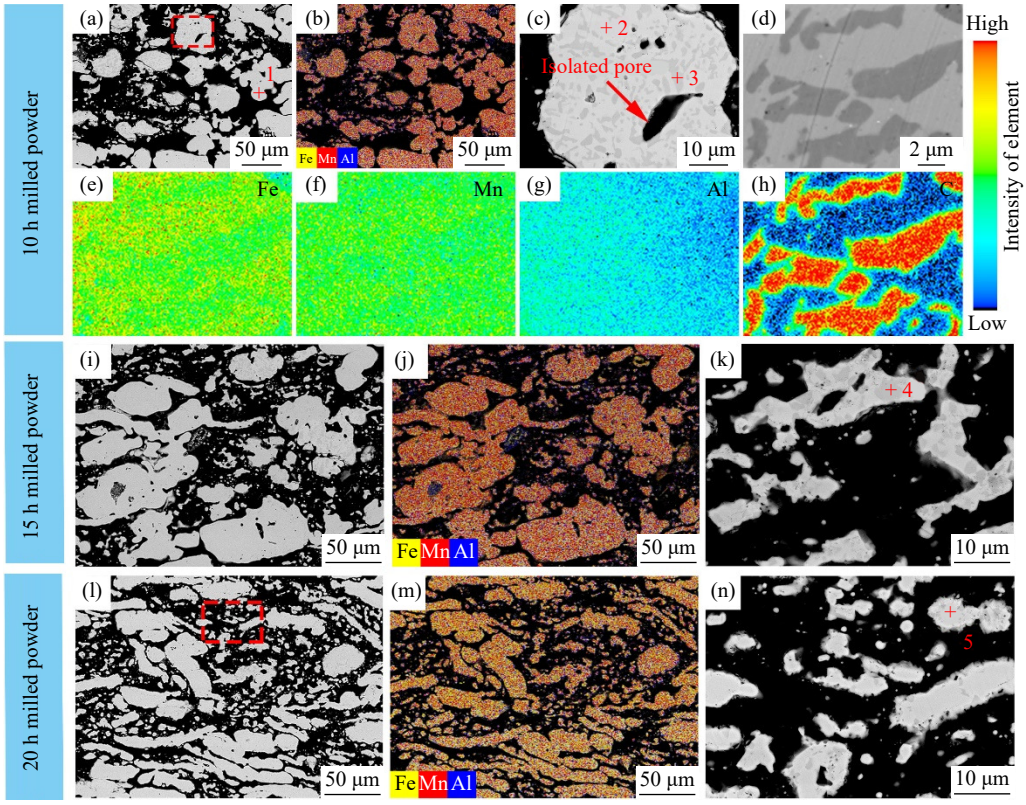

Fig. 8. Microstructure of the milled powder sintered at 1200°C: (a, b) SEM image and EDS result of the sintered 10 h milled powder; (c) enlarged portion in the rectangular box of (a); (d–h) microstructure and corresponding EPMA results; (i, j) SEM image and EDS result of the sintered 15 h milled powder; (k) partial enlarged view of (i); (l, m) SEM image and EDS result of the sintered 20 h milled powder; (n) enlarged portion in the rectangular box of (l).

Table 1. Chemical composition of each point in Fig. 8

Point	Fe / wt%	Mn / wt%	Al / wt%	C / wt%	Possible phase
1	57.04	33.70	7.77	1.49	γ-Fe
2	49.73	38.92	10.83	0.52	γ-Fe
3	48.93	36.13	11.05	3.88	$(Fe,Mn)_3AlC$
4	53.00	31.76	11.12	4.12	$(Fe,Mn)_3AlC$
5	58.91	33.00	6.15	1.94	γ-Fe

3.3. Porosity evolution

As can be seen from Fig. 11(a) and (b), the total and open porosity of the powder decreased continuously at 640 and 1200°C with the extension of milling duration. For example, the total and open porosity of the 10 h milled samples were ~46.6vol% and ~35.2vol% at 640°C, and that of the 20 h milled samples decreased to ~44.2vol% and ~32.7vol%. When sintered at 1200°C, the total and open porosity of the 10 h milled samples were ~58.3vol% and ~55.0vol%, and that of the 20 h milled samples decreased to ~51.3vol% and ~47.2vol%. Previous study revealed that the pores formed at 640°C was mainly caused by the unbalanced diffusion and the chemical reaction between Al and other elements [2,36–37], where the elemental Al particles gradually consumed, and eventually leaving pores at the positions originally occupied by Al particles. In our case, longer ball milling duration resulted in smaller Al particle size and larger surface energy, which effectively reduced the unbalanced diffusion/reaction between Al and other elements, and therefore less pores leaving behind the original sites for the elemental Al particles. In the meanwhile, defects such as vacancies and dislocations in the powder lattice caused by milling, could also provide large driving force to intensify the diffusion and reaction between different elements. This promoted the densification and gave rise to the shrinkage of the pores. Thus, the porosities in both the 640 and 1200°C sintered samples decreased with the increase of milling time. It is also noted that the porosity of the samples sintered at 1200°C was much larger than 640°C, especially the open porosity (see Fig. 11 (b)). This may be attributed to Mn sublimation. The Mn vapor pressure is ~78 Pa at 1200°C, while it is only ~9.5×10^{-5} Pa at 640°C [37]. In our case, the vacuum in the furnace during sintering was ~5×10^{-3} Pa. This implied that the sublimation of Mn at 640°C was inhibited, and that at 1200°C could be very large. It is common that vapors including Mn vapor trapped in the pores could prevent the shrinkage of the pores. Thus, the porosity at 1200°C was higher than 640°C. In addition, transient liquid phases formed during sintering also contributed to the increase of porosity.

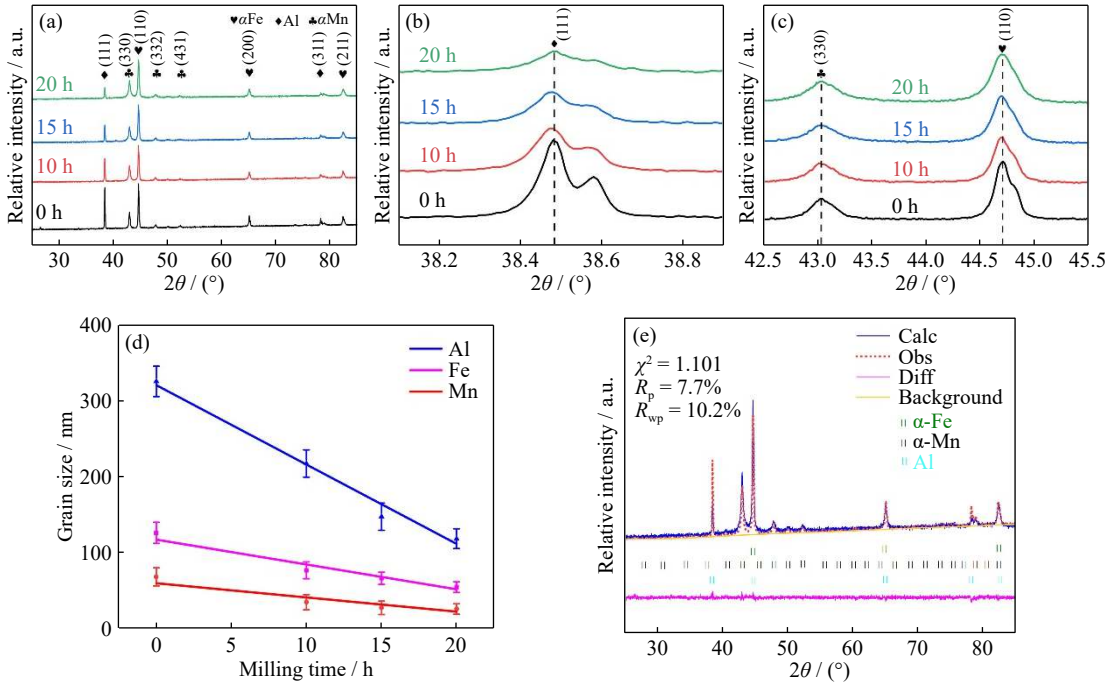

Fig. 9. XRD patterns and the Rietveld refinement of the powder mixtrue for different milling durations: (a) full XRD patterns; (b, c) close view of 38°–39° and 42.5°–45.5°, respectively; (d) calculated grain size of the powder; (e) Rietveld refinement of the 20 h milled powder mixture.

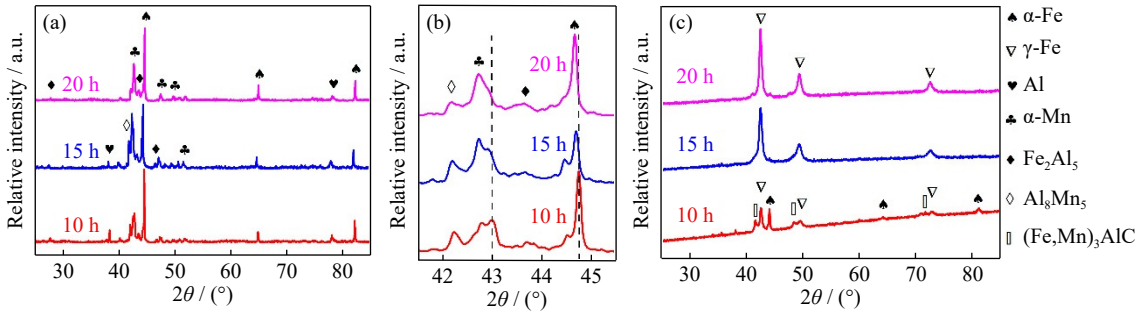

Fig. 10. XRD patterns of the milled powder: (a) sintered at 640°C; (b) close view of 40.5°–46°; (c) sintered at 1200°C.

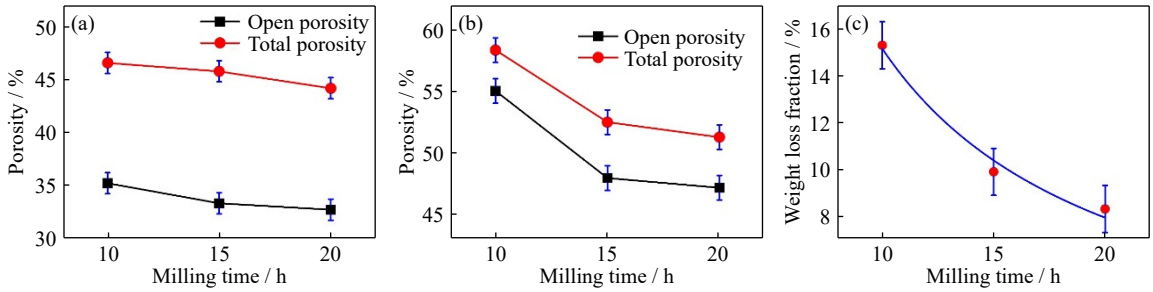

Fig. 11. Relationship between porosity and milling time for sintered at (a) 640°C and (b) 1200°C; (c) weight loss fraction of the samples sintered at 1200°C as a function of milling time.

3.4. Sublimation behavior of Mn

Fig. 11(c) revealed that the weight loss fraction of the sintered compacts at 1200°C decreased with the increase of milling duration. For example, the weight loss fraction of the powder milled for 10 h was ~15.3wt%, while that milled for 20 h remarkably decreased to ~8.3wt%. In order to further explore the influence of ball milling duration on Mn sublimation, EDS point scanning was carried out from the top surface to the interior of the sintered sample, as shown in Fig. 12(a)–(c). In general, Mn content on the surface was less than 2wt%, and it gradually increased from the surface to the core and formed a Mn depletion region (MDR). The MDR for the 10, 15, and 20 h milled samples was about 780, 600, and 370 μm, respectively (Fig. 12(d)–(f)), demonstrating that the longer the powder ball milling duration was, the less Mn sublimation of the sintered samples was, which was consistent with the weight loss fraction results shown in Fig. 11(c). The

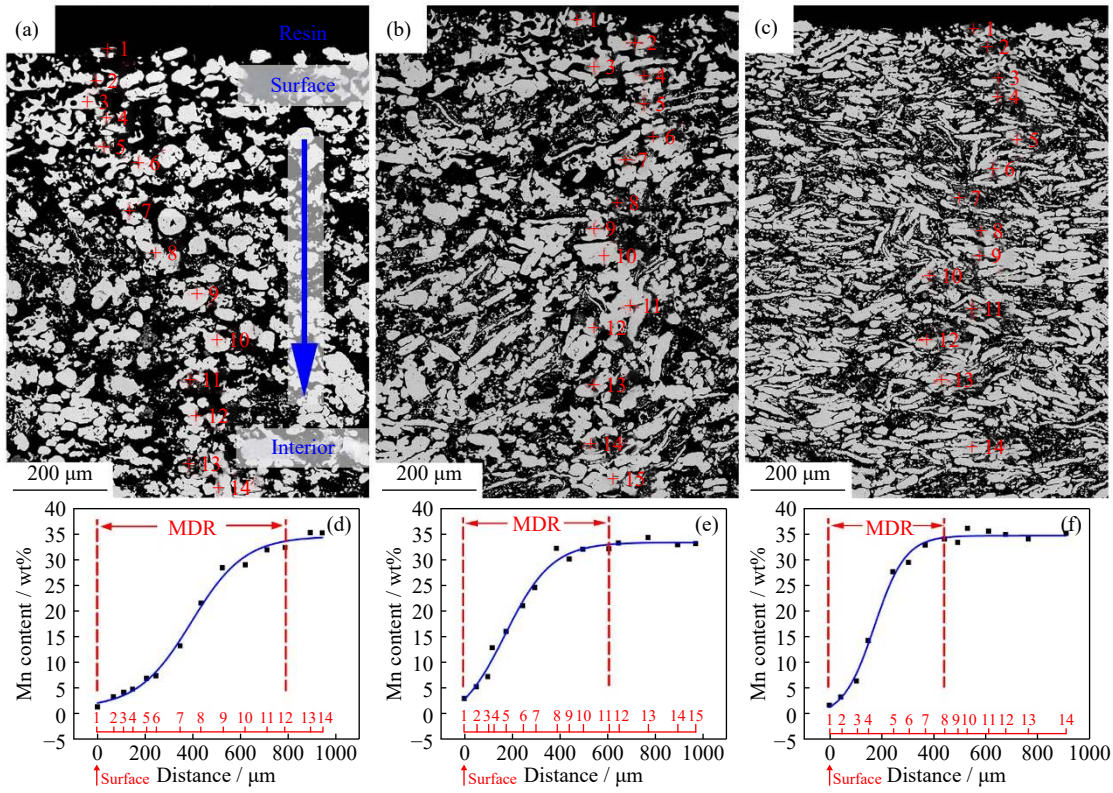

Fig. 12. Cross-section morphologies and EDS point scanning of the milled powder after sintering at 1200°C: (a, d) 10 h; (b, e) 15 h; (c, f) 20 h.

decrease in MDR and the weight loss may be attributed to the decrease of the powder size and open porosity of the sintered samples as a function of milling time. The sublimation of Mn was closely related to the number of open pores, as higher open porosity could provide more sublimation surface and open channels for Mn sublimation. Previous studies have shown that the sintered Fe–Mn–Al–C samples presented limited weight loss after sintering at 640°C, while serious Mn sublimation occurred for the 1200°C sintered samples because of the high Mn vapor pressure up to 78.1 Pa [2,37]. Fig. 11(a) showed that the open porosity of the 640°C sintered samples obviously decreased with the extension of the sintering duration, resulting in less Mn sublimation at 1200°C with the extension of milling duration. In addition, long milling duration greatly increased the sintering driving force for densification, which further reduced the porosity, especially open porosity, so that the sublimation of Mn was inhibited again.

3.5. Compression test

Fig. 13 showed the compression images of the 1200°C sintered porous steels produced by powder milled for 10, 15, and 20 h at different strain stages. In general, the strain for macroscopic crack initiation increased with the prolonged milling time. In detail, tiny cracks initiated on the surface of the compressed samples when the strain reached 30% for the 10 h milled samples (Fig. 13(A4)), 37% for the 15 h milled samples (Fig. 13(B4)), and 50% for the 20 h milled samples ((Fig. 13(C4)). The cracks propagated and grew up as the strain increased, resulting in the surface layers peeling off from the samples at the strain of 35% for the 10 h milled samples (Fig. 13(A6)) and 43% for the 15 h milled sample (Fig. 13(B6)). However, for the 20 h milled samples, no spalling occurred on the surface during the whole compression stages. The sublimation of Mn may be an important reason for this phenomenon. Previous results revealed that Mn contributed to the formation of austenite phase with good ductility [2,4]. Nevertheless, Mn sublimation resulted in the drop of Mn concentration in the Fe-matrix, which was more likely to facilitate the generation of α-Fe phase with poor ductility. The result in Fig. 12 revealed that MDR in the sintered samples prepared by 10 and 15 h milled powder was wide, leading to large α-Fe region on the surface and causing the separation of the surface layer to the sintered samples. On the contrary, the α-Fe region in the sintered samples prepared by 20 h milled powder was significantly reduced due to its low MDR, so its plastic deformation ability was strengthened. Fig. 14 showed the stress-strain curves of the sintered samples. The stress at the microcrack initiation strain for the sintered samples prepared by 10, 15, and 20 h milled powder was about 80, 210, and 470 MPa, respectively. The increase of the compressive strength was closely related to the milling duration. This was because long milling duration was beneficial to the reduction in porosity, as shown in Fig. 11(a) and (b). Finally, higher compressive strength was achieved with longer milling time.

It is noted that the strain for macroscopic crack initiation increased as a function of ball milling time. This means that long ball milling time is in favor of better plasticity. In order to explore the fracture mode of the 1200°C sintered samples

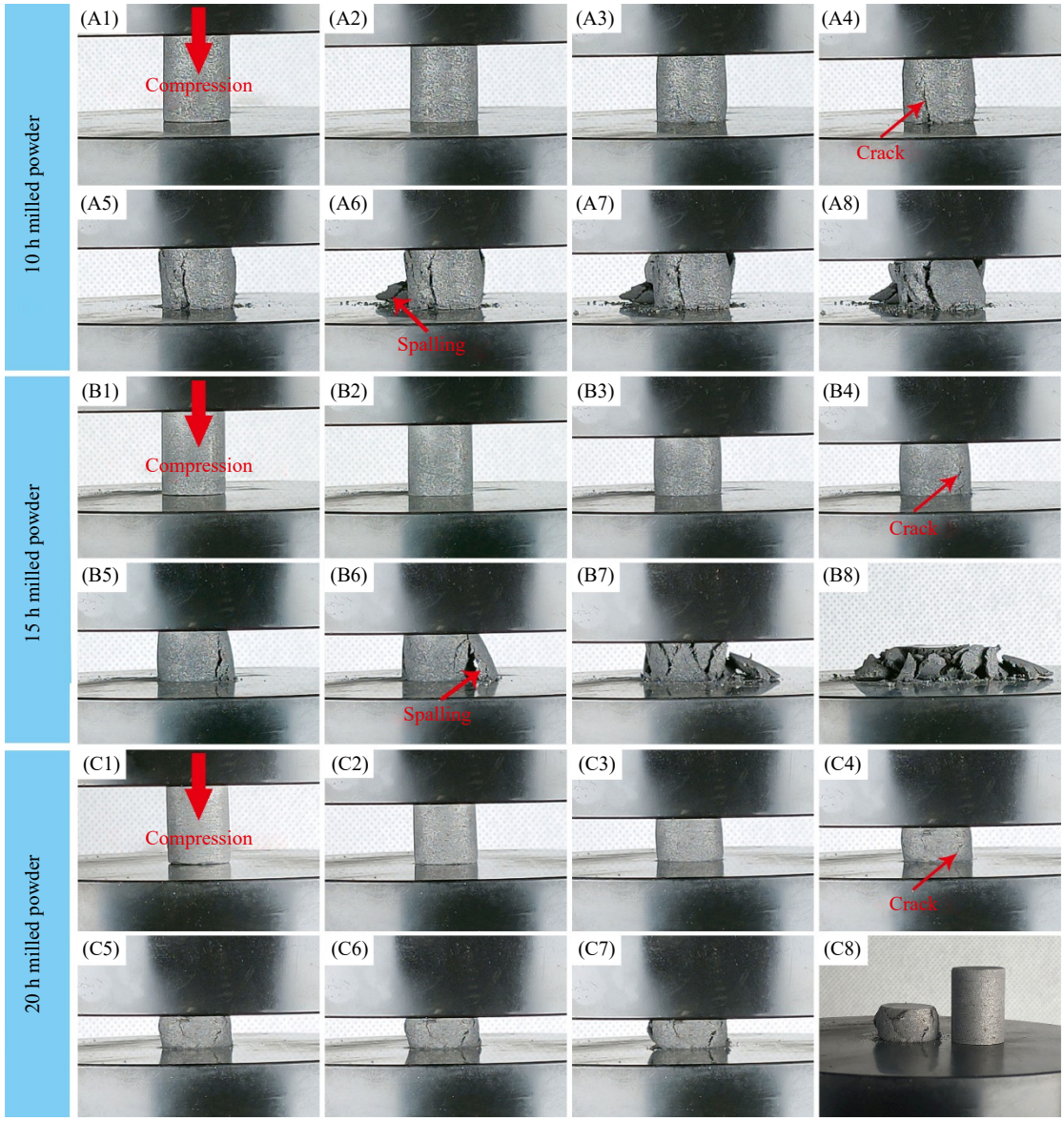

Fig. 13. Macroscopic compression images of the 1200°C sintered porous steels for the (A) 10, (B) 15, and (C) 20 h milled powder at different strain stages: (A1) 0; (A2) 10%; (A3) 25%; (A4) 30%; (A5) 32%; (A6) 35%; (A7) 40%; (A8) 45%; (B1) 0; (B2) 15%; (B3) 30%; (B4) 37%; (B5) 39%; (B6) 43%; (B7) 53%; (B8) end of compression; (C1) 0; (C2) 20%; (C3) 40%; (C4) 50%; (C5) 53%; (C6) 55%; (C7) 57%; (C8) end of compression.

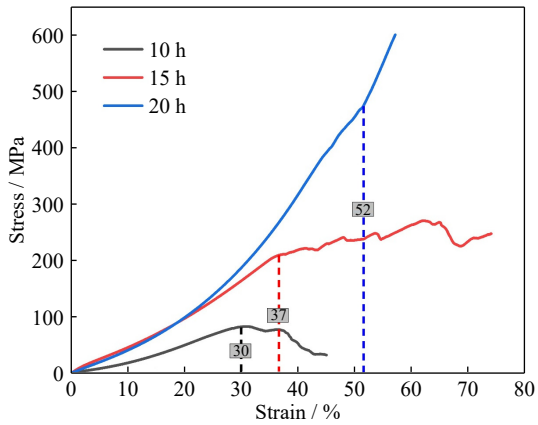

Fig. 14. Compressive stress-strain curves of the 1200°C sintered samples made of the powder with different milling durations.

with different milling time, the fracture morphologies were observed. As shown in Fig. 15, a small number of dimples appeared at the fracture surface of the 10 h milled samples, which proved that plastic deformation occurred at certain sites. However, Fig. 15(c) and (d) presented that looped cracks as the crack initiation were found in the core of the broken Fe-matrix particles, and the fractured surface beyond the loop was smooth, which demonstrated the brittle fracture mode. Long cracks were penetrated the Fe-matrix particles (Fig. 15(e) and (f)), which was a typical transgranular fracture. This also confirmed that a great deal of brittle fracture existed in the 10 h milled samples. In addition, the penetrated microcracks (Fig. 15(g)) caused by the shearing and sliding of the particles were also found in the fractured surface. In general, brittle facture played an essential role in the failure of the samples prepared by 10 h milled powder. Consequently, the broken fragments were compacted with the increased strain,

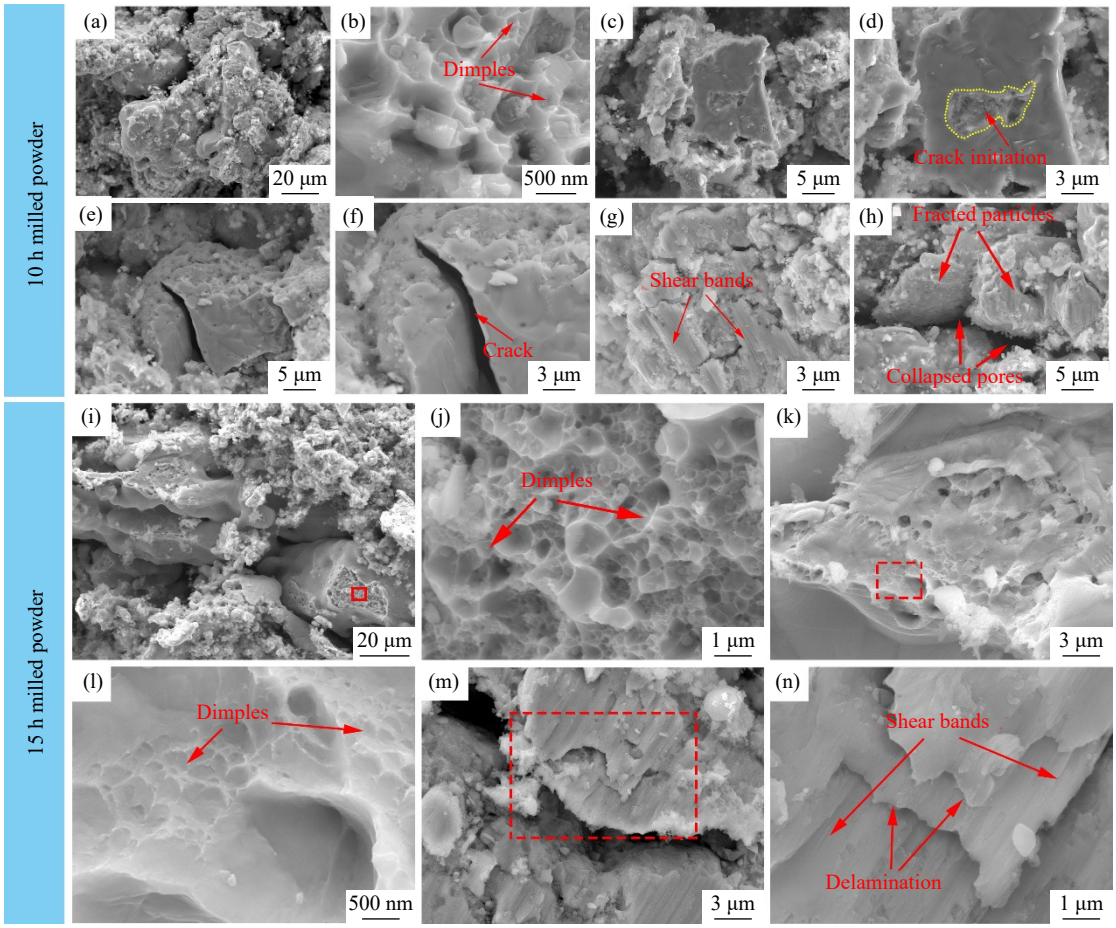

Fig. 15. Fracture morphologies of the porous steel sintered at 1200°C prepared by different milling time: (a) morphology of 10 h; (b) dimples of 10 h; (c) crack initiation of 10 h; (d) enlargement of (c); (e) crack of 10 h; (f) enlargement of (e); (g) shear bands of 10 h; (h) collapsed pores of 10 h; (i) morphology of 15 h; (j) dimples of 15 h; (k) quasi-cleavage fracture of 15 h; (l) enlargement of the red box in (k); (m) shear bands of 15 h; (n) enlargement of the red box in (m).

and pores collapsed, as shown in Fig. 15(h). As the milling time increased to 15 h, larger and deeper dimples were found in more fractured sites (Fig. 15(j)), indicating that more ductile fracture occurred with the extension of the milling time. It is noted that dimples and cleavage planes coexisted at the fracture surface of the 15 h milled samples, indicating that the fracture was quasi-cleavage, as shown in Fig. 15(k) and (l). Similarly, a large number of delaminated fragments were observed in the 15 h milled samples because of the shear force caused by continuous compression.

4. Conclusions

In this work, the effect of ball milling time on the microstructure, phase composition, and compressive properties of the sintered porous steel were discussed. The following conclusions could be drawn.

(1) The particle size of the powder decreased and the morphology of the Fe particles transformed into the laminated structure with the increase of milling time. No phase transformations occurred in the milled powder, and Fe_2Al_5 and Al_8Mn_5 were observed in the compacts sintered at 640°C. After sintering at 1200°C, the 10 h milled powder compacts was mainly composed of γ-Fe and α-Fe, while the 15 and 20 h milled powder compacts was dominated by γ-Fe.

(2) In general, the overall and open porosities of sintered samples decreased with the increase of milling duration at both 640 and 1200°C. When the samples were sintered at 640°C, the overall and open porosity slightly decreased from ~46.6vol% and 35.2vol% for the 10 h milled powder compacts to ~44.2vol% and 32.7vol% for the 20 h milled powder compacts. After sintering at 1200°C, the overall and open porosities of the samples remarkably decreased from ~58.3vol% and 55.0vol% for the 10 h milled powder compacts to ~51.3vol% and 47.2vol% for the 20 h milled powder compacts.

(3) Milling time played a significant impact on the compressive properties of the sintered samples. The strain for macroscopic crack initiation increased from 30% for the 10 h milled powder compacts to 50% for the 20 h milled powder compacts, and the corresponding stress increased from ~80 to ~470 MPa. It is also found that the ductility improved as a function of milling time.

Acknowledgements

This work was financially supported by the National Key R&D Program of China (No. 2021YFB3802300), the Na-

tional Natural Science Foundation of China (No. 51804239), and Guangdong Major Project of Basic and Applied Basic Research, China (No. 2021B0301030001).

Conflict of Interest

The authors declare no potential conflict of interest.

References

[1] A.C. Kaya, P. Zaslansky, M. Ipekoglu, and C. Fleck, Strain hardening reduces energy absorption efficiency of austenitic stainless steel foams while porosity does not, *Mater. Des.*, 143(2018), p. 297.

[2] Z.G. Xu, J.H. Du, C. Zhuang, S.Y. Huang, C.B. Wang, and Q. Shen, Evolution of aluminum particle-involved phase transformation and pore structure in an elemental Fe–Mn–Al–C powder compact during vacuum sintering, *Vacuum*, 175(2020), p. 109289.

[3] M. Su, Q. Zhou, and H. Wang, Mechanical properties and constitutive models of foamed steels under monotonic and cyclic loading, *Constr. Build. Mater.*, 231(2020), p. 116959.

[4] Z.G. Xu, J.R. Liang, Y.M. Chen, W.J. Li, C.B. Wang, and Q. Shen, Sintering of a porous steel with high-Mn and high-Al content in vacuum, *Vacuum*, 196(2022), p. 110746.

[5] I. Mutlu and E.Oktay, Corrosion behaviour and microstructure evolution of 17-4 PH stainless steel foam, *Corros. Rev.*, 30(2012), No. 3-4, p. 125.

[6] S. Bobaru, V. Rico-Gavira, A. García-Valenzuela, C. López-Santos, and A.R.González-Elipe, Electron beam evaporated *vs*. magnetron sputtered nanocolumnar porous stainless steel: Corrosion resistance, wetting behavior and anti-bacterial activity, *Mater. Today Commun.*, 31(2022), p. 103266.

[7] X.Q. Ni, D.C. Kong, Y. Wen, *et al*., Anisotropy in mechanical properties and corrosion resistance of 316L stainless steel fabricated by selective laser melting, *Int. J. Miner. Metall. Mater.*, 26(2019), No. 3, p. 319.

[8] A. Rabiei, K. Karimpour, D. Basu, and M.Janssens, Steel-steel composite metal foam in simulated pool fire testing, *Int. J. Therm. Sci.*, 153(2020), p. 106336.

[9] C.H. Wang, F.C. Jiang, S.Q. Shao, T.M. Yu, and C.H. Guo, Acoustic properties of 316L stainless steel hollow sphere composites fabricated by pressure casting, *Metals*, 10(2020), No. 8, p. 1047.

[10] X.B. Xu, P.S. Liu, G.F. Chen, and C.P. Li, Sound absorption performance of highly porous stainless steel foam with reticular structure, *Met. Mater. Int.*, 27(2021), No. 9, p. 3316.

[11] H. Jain, R. Kumar, G. Gupta, and D.P. Mondal, Microstructure, mechanical and EMI shielding performance in open cell austenitic stainless steel foam made through PU foam template, *Mater. Chem. Phys.*, 241(2020), p. 122273.

[12] T.Y. Lim, W. Zhai, X. Song, *et al*., Effect of slurry composition on the microstructure and mechanical properties of SS316L open-cell foam, *Mater. Sci. Eng. A*, 772(2020), p. 138798.

[13] Y. Guo, M.C. Zhao, B. Xie, *et al., In vitro* corrosion resistance and antibacterial performance of novel Fe–*x*Cu biomedical alloys prepared by selective laser melting, *Adv. Eng. Mater.*, 23(2021), No. 4, p. 2001000.

[14] S. Yiatros, O. Marangos, R.A. Votsis, and F.P. Brennan, Compressive properties of granular foams of adhesively bonded steel hollow sphere blocks, *Mech. Res. Commun.*, 94(2018), p. 13.

[15] H. Sazegaran and S.M.M. Nezhad, Cell morphology, porosity, microstructure and mechanical properties of porous Fe–C–P alloys, *Int. J. Miner. Metall. Mater.*, 28(2021), No. 2, p. 257.

[16] C. Mapelli, D. Mombelli, A. Gruttadauria, S. Barella, and E.M. Castrodeza, Performance of stainless steel foams produced by infiltration casting techniques, *J. Mater. Process. Technol.*, 213(2013), No. 11, p. 1846.

[17] K. Alvarez, K. Sato, S.K. Hyun, and H. Nakajima, Fabrication and properties of Lotus-type porous nickel-free stainless steel for biomedical applications, *Mater. Sci. Eng. C*, 28(2008), No. 1, p. 44.

[18] C. Garcia-Cabezon, C. Garcia-Hernandez, M.L. Rodriguez-Mendez, and F.Martin-Pedrosa, A new strategy for corrosion protection of porous stainless steel using polypyrrole films, *J. Mater. Sci. Technol.*, 37(2020), p. 85.

[19] M. Mokhtari, T. Wada, C. Le Bourlot, *et al*., Corrosion resistance of porous ferritic stainless steel produced by liquid metal dealloying of Incoloy 800, *Corros. Sci.*, 166(2020), No. 7, p. 108468.

[20] Y.B. Ren, J. Li, and K. Yang, Preliminary study on porous high-manganese 316L stainless steel through physical vacuum dealloying, *Acta Metall. Sin.*, 30(2017), No. 8, p. 731.

[21] D.C. Kong, X.Q. Ni, C.F. Dong, *et al*., Anisotropy in the microstructure and mechanical property for the bulk and porous 316L stainless steel fabricated via selective laser melting, *Mater. Lett.*, 235(2019), p. 1.

[22] Y. Zhu, G.L. Lin, M.M. Khonsari, J.H. Zhang, and H.Y. Yang, Material characterization and lubricating behaviors of porous stainless steel fabricated by selective laser melting, *J. Mater. Process. Technol.*, 262(2018), p. 41.

[23] H.Y. Chen, D.D. Gu, Q. Ge, *et al*., Role of laser scan strategies in defect control, microstructural evolution and mechanical properties of steel matrix composites prepared by laser additive manufacturing, *Int. J. Miner. Metall. Mater.*, 28(2021), No. 3, p. 462.

[24] K. Li, J.B. Zhan, T.B. Yang, *et al*., Homogenization timing effect on microstructure and precipitation strengthening of 17-4PH stainless steel fabricated by laser powder bed fusion, *Addit. Manuf.*, 52(2022), art. No. 102672.

[25] Z.Y. Liu, S.J. Xu, B.L. Xiao, P. Xue, W.G. Wang, and Z.Y. Ma, Effect of ball-milling time on mechanical properties of carbon nanotubes reinforced aluminum matrix composites, *Composites Part A*, 43(2012), No. 12, p. 2161.

[26] F. Ghadami, A.S.R. Aghdam, and S. Ghadami, Characterization of MCrAlY/nano-Al_2O_3 nanocomposite powder produced by high-energy mechanical milling as feedstock for high-velocity oxygen fuel spraying deposition, *Int. J. Miner. Metall. Mater.*, 28(2021), No. 9, p. 1534.

[27] S.A. Hewitt and K.A. Kibble, Effects of ball milling time on the synthesis and consolidation of nanostructured WC–Co composites, *Int. J. Refract. Met. Hard Mater.*, 27(2009), No. 6, p. 937.

[28] A. Nouri, P.D. Hodgson, and C. Wen, Effect of ball-milling time on the structural characteristics of biomedical porous Ti–Sn–Nb alloy, *Mater. Sci. Eng. C*, 31(2011), No. 5, p. 921.

[29] R. Raimundo, R. Reinaldo, N. Câmara, *et al*., Al_2O_3–10wt% Fe composite prepared by high energy ball milling: Structure and magnetic properties, *Ceram. Int.*, 47(2021), No. 1, p. 984.

[30] C. Garcia-Cabezon, Y. Blanco, M. Rodriguez-Mendez, and F. Martin-Pedrosa, Characterization of porous nickel-free austenitic stainless steel prepared by mechanical alloying, *J. Alloys Compd.*, No.(2017), p. 46.

[31] N. Bekoz and E. Oktay, The role of pore wall microstructure and micropores on the mechanical properties of Cu–Ni–Mo based steel foams, *Mater. Sci. Eng. A*, 612(2014), p. 387.

[32] G. Castro, S.R. Nutt, and X.W. Chen, Compression and low-velocity impact behavior of aluminum syntactic foam, *Mater. Sci. Eng. A*, 578(2013), p. 222.

[33] K. Kato, A. Yamamoto, S. Ochiai, *et al*., Cytocompatibility and mechanical properties of novel porous 316L stainless steel, *Mater. Sci. Eng. C*, 33(2013), No. 5, p. 2736.

[34] D.P. Mondal, H. Jain, S. Das, and A.K. Jha, Stainless steel foams made through powder metallurgy route using NH_4HCO_3 as space holder, *Mater. Des.*, 88(2015), p. 430.
[35] K.G. Chin, H.J. Lee, J.H. Kwak, J.Y. Kang, and B.J. Lee, Thermodynamic calculation on the stability of $(Fe, Mn)_3AlC$ carbide in high aluminum steels, *J. Alloys Compd.*, 505(2010), No. 1, p. 217.
[36] Z.G. Xu, J.R. Liang, and J.H. Du, The microstructure and compressive properties of a sintered Fe–Mn–Al porous steel produced by blended elemental powder mixture, *Int. J. Mod. Phys. B*, 36(2022), No. 12-13, p. 2240058.
[37] C.B. Zhuang, Z.G. Xu, S.Y. Huang, Y. Xia, C.B. Wang, and Q. Shen, *In situ* synthesis of a porous high-Mn and high-Al steel by a novel two-step pore-forming technique in vacuum sintering, *J. Mater. Sci. Technol.*, 39(2020), p. 82.
[38] L.H. Zhou, Z. Li, S.S. Wang, *et al*., Calculation of phase equilibria in Al–Fe–Mn ternary system involving three new ternary intermetallic compounds, *Adv. Manuf.*, 6(2018), No. 2, p. 247.
[39] A.T. Phan, M.K. Paek, and Y.B. Kang, Phase equilibria and thermodynamics of the Fe–Al–C system: Critical evaluation, experiment and thermodynamic optimization, *Acta Mater.*, 79(2014), p. 1.
[40] B. Hallstedt, A.V. Khvan, B.B. Lindahl, M. Selleby, and S. Liu, PrecHiMn-4—A thermodynamic database for high-Mn steels, *Calphad*, 56(2017), p. 49.
[41] W.S. Zheng, S. He, M. Selleby, *et al*., Thermodynamic assessment of the Al–C–Fe system, *Calphad*, 58(2017), p. 34.
[42] M.S. Kim and Y.B.Kang, Development of thermodynamic database for high Mn-high Al steels: Phase equilibria in the Fe–Mn–Al–C system by experiment and thermodynamic modeling, *Calphad*, 51(2015), p. 89.